Noncollinear Relativistic DFT+U Calculations of Actinide Dioxide Surfaces

James T. Pegg,[1,2*] Ashley E. Shields,[3] Mark T. Storr,[2] David O. Scanlon,[1,4,5] and Nora H. de Leeuw.[1,6]

[1] Department of Chemistry, University College London, 20 Gordon Street, London WC1H 0AJ, United Kingdom.

[2] Atomic Weapons Establishment (AWE) Plc, Aldermaston, Reading, RG7 4PR, UK.

[3] Oak Ridge National Laboratory, One Bethel Valley Road, Oak Ridge, Tennessee 37831, USA

[4] Diamond Light Source Ltd., Diamond House, Harwell Science and Innovation Campus, Didcot, Oxfordshire OX11 0DE, United Kingdom.

[5] Thomas Young Centre, University College London, Gower Street, London WC1E 6BT, UK

[6] Cardiff University, School of Chemistry, Main Building, Park Place, Cardiff, CF1D 3AT, United Kingdom.

Corresponding Author James T. Pegg: uccajtp@ucl.ac.uk

Abstract: A noncollinear relativistic PBEsol+U study of the low-index actinide dioxides (AnO_2, An = U, Np, Pu) surfaces has been conducted. The surface properties of the AnO_2 have been investigated and the importance of the reorientation of magnetic vectors relative to the plane of the surface is highlighted. In collinear nonrelativistic surface models, the orientation of the magnetic moments is often ignored; however, the use of noncollinear relativistic methods is key to the design of reliable computational models. The ionic relaxation of each surface is shown to be confined to the first three monolayers and we have explored the configurations of the terminal oxygen ions on the reconstructed (001) surface. The reconstructed (001) surfaces are ordered as (001)αβ < (001)α < (001)β in terms of energetics. Electrostatic potential isosurface and scanning tunneling microscopy images have also been calculated. By considering the energetics of the low-index AnO_2 surfaces, an octahedral Wulff crystal morphology has been calculated.

1 Introduction

The surface chemistry of the actinide dioxides (AnO_2, An = U, Np, Pu) is key to understanding corrosion mechanisms,[1-8] which impacts the design of long-term storage facilities and the industrial reprocessing of nuclear fuels.[9-15] The inexorable oxidation of actinide metal forms an oxide surface layer; where, the composition controls successive corrosion rates.[1-5, 7, 16] The rapid onset of corrosion has resulted in: thermal excursions, failure of containment vessels, and the resulting dispersal of nuclear materials. To reduce the risk of nuclear proliferation and assist in nuclear decommissioning, the controlled oxidation of actinide metals offers a means of converting classified nuclear material to simple ingots.[7] In terms of fuel fabrication, the surface energetics of the AnO_2 impact fuel sintering and particle morphology.[17]

As a result of their inhomogeneous and radioactive nature, few AnO_2 experimental surface studies have been completed.[9, 13, 18-24] To circumvent experimental issues, computational methods offer another mode of study. Although a computational investigation of heavy-fermion systems is also challenging. To investigate the complex electronic structure by computational methods, one must consider exchange-correlation influences, relativistic contributions, and noncollinear magnetic behaviour.[25] Only a limited number of studies have considered relativistic contributions (spin-orbit interaction, SOI); which is important in the treatment of actinide systems.[26-28] In addition, the actinides often have complex (noncollinear) magnetic structures, and thus far no investigation of AnO_2 surfaces has incorporated noncollinear magnetic behavior.[27]

The actinides are highly-correlated *f*-electron systems for which conventional DFT methods calculate an incorrect electronic structure. To model highly-correlated materials correctly, a number of methods have been developed: the self-interaction correction (SIC) method,[29] modified density functional theory (DFT+U),[30-34] dynamic mean field theory (DMFT),[35] and hybrid density functionals.[36-38] As a computationally tractable method, DFT+U offers a means of study in which the electronic structure can be computed. In the Liechtenstein DFT+U formulism, where independent Coulomb (U) and exchange (J) terms treat the on-site Coulomb repulsion of the An *f*-electrons. The values are derived from higher level *ab-initio* methods or obtained through semi-empirical analysis.[26]

The electronic structure of the AnO_2 is influenced by changes in magnetic order;[27] here, the importance of magnetic vector reorientation is highlighted. The effect of transverse 3k AFM behavior on the properties of the UO_2 surface is unknown, whereas investigations on NpO_2 and PuO_2 surfaces are even less common.[9, 11] Information on the low-index AnO_2 (111), (011), (001) surfaces has been calculated by DFT+U: energetics, ionic relaxation, electrostatic isosurfaces, scanning tunneling microscopy (STM) images, crystal morphology, and dipolar reconstructions.

1.1 Magnetic Structure

The magnetic structure of the AnO_2 is highly complicated. A discontinuous first-order magnetic phase transition (T_N = 30.8 K)[39] in UO_2 has been established by heat capacity,[40-41] magnetic susceptibility[42] and neutron diffraction[43-45] measurements. A transverse 3k antiferromagnetic (AFM) ground-state has been identified **(Figure 1)**.[26, 46-47] The ground-state corresponds to an internal $Pa\overline{3}$ (No. 205) crystallographic distortion synonymous with magnetic order (the displacement of the O^{2-} ions is 0.014 Å).[45-46, 48-49]

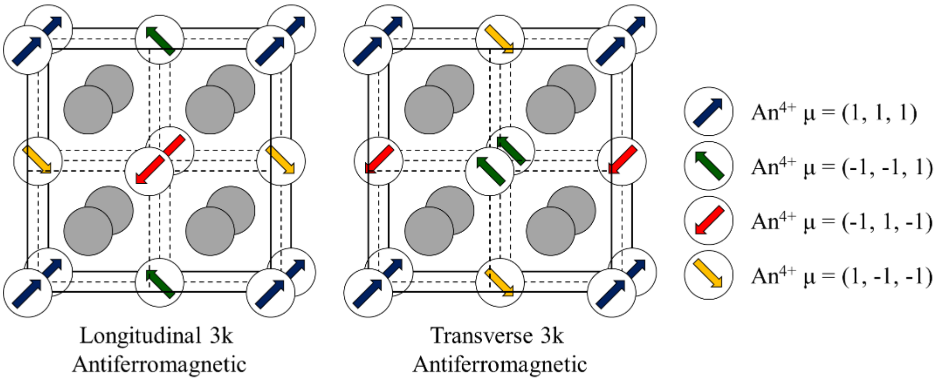

Figure 1: *The longitudinal 3k AFM and transverse 3k AFM phases for the AnO_2 crystal structure.*

The magnetic structure of NpO_2 remains unresolved. In the absence of interactions that break time-reversal symmetry conditions, the Np^{4+} ion (a Kramers ion, one with an uneven number of valence electrons) should order magnetically at low-temperature.[50] A first-order paramagnetic (PM)-AFM phase transition (T = 25.4 K) has been inferred by: magnetic susceptibility[51] and specific heat capacity measurements.[52-53] In-spite of an exhaustive search, a measurable local magnetic moment has not been identified by: low-temperature Mossbauer (T = 1.5 K),[50] neutron diffraction (12 K < T < 30K),[54] and muon spin rotation (0.3 K < T < 25.4 K) measurements.[55-56]

In terms of the crystal structure, no evidence has been found of an external distortion, which would indicate noncollinear 3k AFM order.[53] An internal O^{2-} ion distortion (indicative of transverse 3k AFM behaviour with $Pa\overline{3}$ (No. 205) crystal symmetry) can be inferred from: the small broadening of Mossbauer spectroscopic lines,[50] and inelastic neutron scattering (INS) (5 K < T < 25 K) measurements.[57-58] An internal O^{2-} ion distortion of 0.02 Å has been calculated, which is, however, below the experimental resolution.[53, 56, 59] In contrast, a longitudinal 3k AFM ground-state has been indicated by: resonant X-ray scattering[60] (10 K < T < 17 K) and ^{17}O NMR measurements (T = 17 K).[61] The transverse 3k AFM state, relative to the longitudinal 3k AFM state, is 0.002 eV·formula unit^{-1} lower in energy (as calculated by HSE06 incorporating SOI).

An experimental singlet Γ1 diamagnetic (DM) PuO_2 ground-state has been inferred from: magnetic susceptibility (T = 4 K), inelastic neutron scattering (T > 30 K), and nuclear magnetic resonance (T > 4 K) measurements. However, a number of inconsistencies have been identified, and an ordered magnetic ground-state can be assumed. In contrast to experimental measurements, a longitudinal 3k AFM ground-state has been calculated.[18, 22-24, 38, 62-72] It is thought that PuO_2 could be a small-moment insulator (similar to NpO_2) for which DFT overestimates the magnetic moments. In this study, transverse 3k AFM order (UO_2, NpO_2) and longitudinal 3k AFM order (PuO_2) have been used to describe the crystals.

To model noncollinear magnetic behavior, it is imperative that relativistic effects are considered. A significant number of studies ignore the SOI (important in heavy-fermion systems) to reduce the computational cost.[11, 73-75] A limited number of studies on UO_2[9] and PuO_2[23] consider relativistic contributions to the total energy. The importance of SOI on modeling UO_2 by DFT initially seemed to be inconsequential.[9] In a nonrelativistic treatment of other actinide systems, the study has often been cited to justify the absence of SOI.[9, 23, 73]

The importance of SOI on the PuO_2 (111) surface energies has now been highlighted by hybrid DFT,[23] but all studies have limited themselves to a discussion of collinear 1k AFM order.

A major limitation of scalar calculations is the inability to orient the magnetic moments relative to the direction of the surface. In this manner, the magnetic moments are directed orthogonal to the surface plane, which leads to notable inconsistencies within the electronic structure. If not corrected, the orientation of the magnetic field is also directed orthogonal to the surface plane, because the principal axis differs between the surfaces. Consequently, the electronic, magnetic, and crystal structures differ between the bulk crystal structure and individual surfaces. If the magnetic vectors are not reoriented, the energetics and structural relaxations derived by this approach are incomplete.[27] This is particularly concerning when calculating the surface energy, which is derived from the bulk structure and it is therefore important that the magnetic vectors relative to the surface are carefully reoriented. In past studies where this essential transformation has been omitted, the energies of the bulk and surface are therefore often incomparable, which introduces a significant error when calculating the energy of the surface. In this study, the magnetic vectors are reoriented relative to the surface plane, which ensures that we preserve the noncolinear 3k AFM structure. In addition, the reduction of cubic symmetry associated with collinear 1k AFM states (used in past calculations) is avoided.[27]

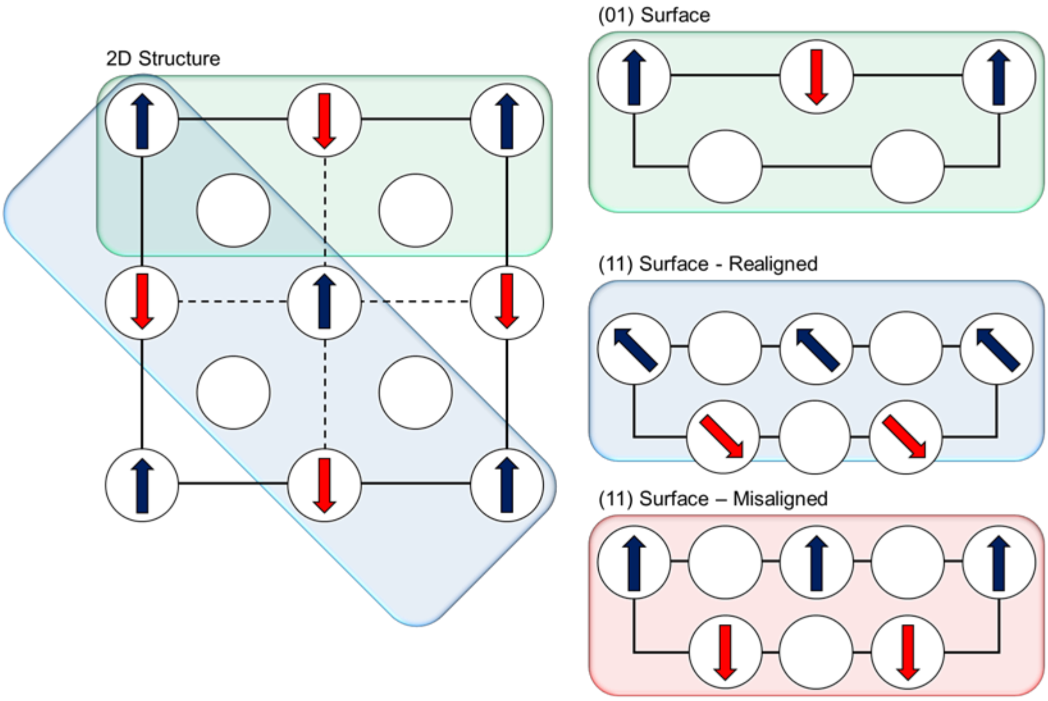

Figure 2: *The surface magnetism of a two-dimensional material. The direction of the magnetic moments for the respective surfaces are shown for the first two layers of the bulk crystal structure. The highlighted (01) (green) and (11) (blue) surfaces correctly emulate the magnetic structure in the bulk crystal. In contrast, the (11) (red) surface illustrates an incorrect depiction where the magnetic moments are aligned orthogonal to the surface.*

The magnetic structure is commonly defined by the principal axis. The principal axis of the AnO_2 (111), (011) surface differs from that of the bulk crystal and the final magnetic, electronic and crystal structures are therefore inequivalent. However, this is not the case for the AnO_2 (001) surface which shares the same axes. To illustrate in a two-dimensional material, we consider the first two layers of a collinear 1k AFM material (**Figure 2**). The (01) surface and the crystal share the same principal axis and the magnetic structures are therefore directly related. In the (11) surface, the principal axis differs from that of the crystal, which results in an unrelated magnetic and electronic structure. It is therefore critical to orient the magnetic vectors to emulate the initial crystal structure.

2 Computational Methodology

2.1 Calculation Details

A noncollinear relativistic computational study of AnO_2 (An = U, Np, Pu) surfaces has been completed with the Vienna *Ab-initio* Simulation Package (VASP).[29, 35, 76] The code uses: planewave basis sets, relativistic effective core potentials (ECPs), and the frozen-core projector-augmented wave (PAW) method. The cut-off energy of the planewave basis set was 500 eV. The uranium ($6s^2$, $7s^2$, $6p^6$, $6d^2$ $5f^2$), neptunium ($6s^2$, $7s^2$, $6p^6$, $6d^2$ $5f^3$), plutonium, ($6s^2$, $7s^2$, $6p^6$, $6d^2$ $5f^4$) and oxygen ($2s^2$, $2p^4$) valence electrons have been explicitly considered. The integration over the Brillouin zone was completed with the Blöchl tetrahedron method and a Γ-centered k-point grid.[77-78] The influence of the SOI[73] and noncollinear magnetic wave-vectors have been considered. As a correction to the total energy, the SOI is included as a final perturbation. In the treatment of the SOI term, a few assumptions are made. First, a complete basis set is formed within the PAW spheres, and the SOI outside of the PAW spheres is irrelevant.[73] Second, the wave functions are solutions of the radial scalar relativistic Schrödinger equation, which includes Darwin and mass-velocity terms. The spin quantization axis is defined by the (001) plane, from which magnetic and spinor-like values are calculated.

The on-site Coulomb repulsion of the An 5*f* electrons has been treated by the Liechtenstein et. al. DFT+U[32-34] formulism.[33] In the Liechtenstein et. al. formulism, the Coulomb (U) and exchange (J) modifiers are treated as independent variables.[33] To correctly calculate the electronic structure of the AnO_2 (where conventional methods often fail), the Coulomb modifier has been chosen to emulate the experimental band-gap. The uranium (U = 3.35 eV), neptunium (U = 4.25 eV), and plutonium (U = 6.00 eV) Coulomb modifiers are shown. The influence of J on noncollinear magnetic materials has been investigated.[26-27, 79] The anisotropic nature of the f-states has been shown to increases with J (and with U), and therefore J is ignored in this study.[26, 79-80] The selected conditions offer an accurate representation of the electronic structure. The exchange-correlation energy has been evaluated by the revised Perdew-Burke-Ernzerhof for solids (PBEsol) functional.[30-31, 81] The iteration threshold for electronic and ionic convergence has been set at $1x10^{-5}$ eV and $1x10^{-2}$ eV $Å^{-1}$, respectively. As the crystal and electronic structures of AnO_2 are highly dependent on the magnetic state, it is imperative to correctly reorientate the magnetic vectors with respect to the surface plane.

Ionic relaxation is a common mechanism by which the surface energy is minimized with respect to the unrelaxed surface. The surface energy (γ) is a measure of the surface stability and is defined by:

$$\gamma = \frac{E_{tot}(N) - N \cdot E_{AnO_2}}{2A} \tag{1}$$

The number of formula units (N), the total energy of the surface slab, ($E_{tot}(N)$) and the total energy per formula unit (E_{AnO_2}) are defined in the parentheses. In our calculations, all ions are relaxed while the dimensions of the unit cell are fixed. The conjugate gradient method has been employed in the relaxation of the ions. Images are visualized by the Crystal Maker[82] and VESTA codes.[83] The density of states have been illustrated by the SUMO code, a command-line plotting tool for ab-initio calculations.

2.2 Low-Index Surface Models

The low-index AnO_2 (111), (011), (001) surfaces are created by the METADISE code (**Figure 3**)[84] from the ionically relaxed crystal structure. The nonpolar (111) surface is comprised of charged O-An-O monolayers; whereas, the dipolar (011) surface is comprised of charge neutral planes.

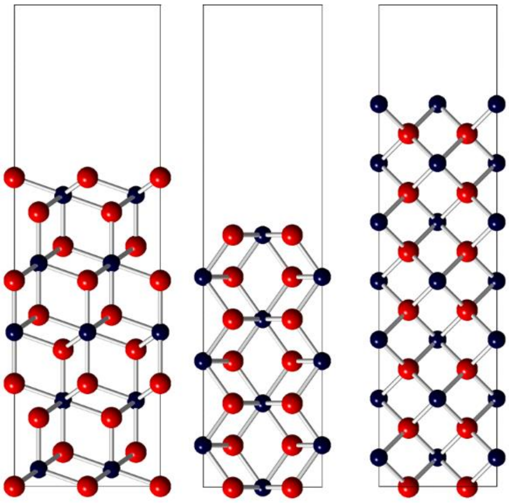

Figure 3: *The low-index AnO_2 (111), (011), (001) surfaces of an ideal calcium fluoride (CaF_2) structural motif. The oxygen (red) and actinide (blue) ions are indicated.*

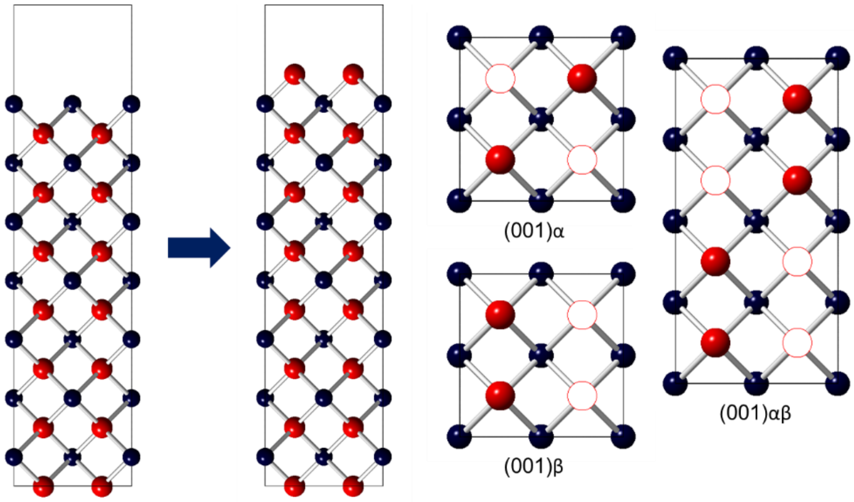

Figure 4: *The low-index AnO_2 (001) to (001)r surface reconstruction. In a (1·1) unit cell, the transposition of oxygen ions results in the (001)α or (001)β configurations. In a (1·2) unit cell, the transposition of oxygen ions results in the (001)αβ configuration. The oxygen (red), oxygen vacancies (white), and actinide (blue) ions are indicated.*

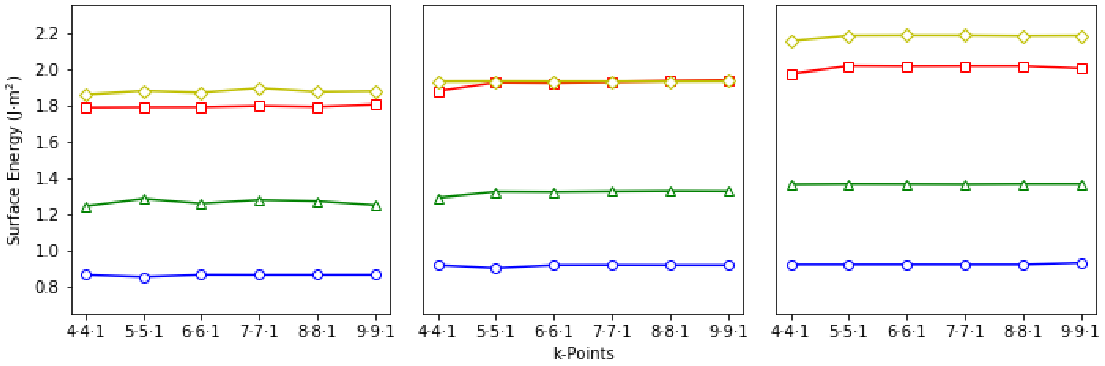

Figure 5: *The surface energy is converged with respect to the k-point grid for each surface: a) uranium dioxide, b) neptunium dioxide, c) plutonium dioxide. The colors in the parentheses indicate the (111) (Green), (011) (Blue), (001)α (Red) and (001)β (Yellow) surfaces. In these calculations, the (111), (001)α, (001)β surfaces are formed of 15 monolayers; whereas the (011) surface is formed of 7 monolayers.*

The polar (001) surface (formed of dipolar An-O layers) is inherently unstable.[17, 85-86] The electrostatic energy relative to the number of monolayers diverges; this is driven by the electric dipole moment.[87-88] To eliminate the dipole moment the surface undergoes a reconstruction, whereby half of the charge oxygen ions are transposed from one surface to the other. This results in the formation of a half-filled oxygen terminated surface (**Figure 4**). The reconstruction is influenced by environmental conditions in nature.[86, 89] In the non-polar reconstructed (001)r surface, the (001)α or (001)β configurations in a (1·1) unit cell can be formed. Although numerous configurations are possible in a (1·2) unit cell, the (001)αβ reconstruction offers a hybridization between the two (1·1) reconstructions, and in this study we have calculated the relative stabilities of these three surface configurations.

The surface energy is converged with respect to the k-point grid to under 0.05 J m^{-2} (**Figure 5**). The (111) surface is calculated from a 5·5·1 Γ-centered k-point grid recommended for hexagonal structures, whereas the (011) and (001) surfaces are calculated from a 4·4·1 Γ-centered k-point grid.[85] To minimize potential aliasing errors, the initial bulk structure (from which the surfaces are derived) is calculated with both a 4·4·4 and a 5·5·5 Γ-centered k-point grid for direct comparison. Finally, the (001)αβ surface is calculated form a 4·2·1 Γ-centered k-point.

2.3 The HIVE Code

In the scanning tunnelling microscopy (STM) HIVE code,[90-91] the Tersoff-Hamann model is considered, where the tunnelling-current is equivalent to the local density of states.[92] A point source at a constant height (2.5 Å) and a Fermi energy sample bias (-2.50 eV) is used. Topographies calculated by HIVE include: copper,[93] germanium,[90-91] gold,[94] iron oxide,[95] thorium dioxide.[96]

2.4 Wulff Reconstruction

According to the Gibbs thermodynamic principle, the equilibrium crystal morphology is influenced by the total surface energy of the medium interface. An equilibrium crystal morphology that minimises ΔG_i has been calculated as follows (**Equation 3**):

$$\Delta G_i = \sum_j \gamma_j A_j \tag{2}$$

The terms in the parentheses describe the total crystal-medium interface free energy (ΔG_i), the surface Gibbs free energy (γ_j) and the surface area (A_j).

3 Results & Discussion

3.1 Model Constraints

3.1.1 Surface Energetics

As a function of the number of formula units used, the energy of the low-index AnO_2 surfaces has been calculated (**Supporting Information, Figure S1**). The ions are fully relaxed while keeping the relative dimensions of the unit cell fixed. In this study, the surface energy is converged to within 0.01 $J{\cdot}m^{-2}$ when 12 or more formula units are used. The surface energy increases across the series as (111) < (011) < (001)α < (001)β (typical of fluorite-structured materials) (**Table 1**).[87, 96] The energy difference between the (001)α and (001)β terminations are relatively small in UO_2 (0.08 $J\ m^{-2}$) and NpO_2 (0.06 $J\ m^{-2}$), compared to PuO_2 (0.19 $J\ m^{-2}$) . If one uses a (1·1) unit cell model, the (001)α surface relative to the (001)β surface is energetically favourable, which is confirmed independently by an interatomic potential-based investigation on UO_2.[89] Compared with past DFT-based methods, the calculated surface energies are considerably greater for each surface.[9, 11, 17-18, 23, 75, 97] although interatomic potential models[89] and relativistic hybrid calculations[15] of UO_2 have resulted in even higher surface energies.

Table 1: *The Relaxed Energy ($J{\cdot}m^{-2}$) of the AnO_2 (111), (011), (001) Surfaces.*

	(111)	(011)	(001)		
			(001)α	(001)β	(001)αβ
UO_2	0.85	1.23	1.75	1.83	1.69
NpO_2	0.90	1.28	1.86	1.92	1.80
PuO_2	0.92	1.35	1.96	2.13	1.85

In addition, interatomic potential models of UO_2 have calculated lower-energy (001) surface reconstructions, which are formed using a larger unit cell.[89, 98] In the reconstruction of the (001) surface in our (1·1) unit cell, only the (001)α and (001)β configurations can be generated, whereas the surface energy of the (001)αβ configuration from a (1·2) unit cell (calculated using 28 formula units) relative to the (001)α and (001)β configurations, is considerably lower in energy (**Table 1**). This implies a limitation of the DFT (1·1) unit cell model and it is clearly possible that other configurations, in even larger cells, could be more stable. However, increasing the size of the cell increases the computational cost of the system significantly, and a systematic fully relativistic DFT study of bigger simulations cells is currently computationally intractable.

3.1.2 Ionic Relaxation

The low-index AnO_2 surfaces are characterized by the changes in the interlayer spacings (**Figure 6a-6d & Figure 7a-7d**), which enables a quantitative analysis of the structural relaxation between layers. The interlayer relaxation ($\Delta d_{interlayer}$) is calculated by:

$$\Delta d_{interlayer} = (d_{i,i+1})_{relaxed} - d_{unrelaxed} \quad (3)$$

where $(d_{i,i+1})_{relaxed}$ is the average interlayer separation of ions in the relaxed surface and $d_{unrelaxed}$ is the average interlayer separation of ions in the unrelaxed surface. The interlayer relaxation is reminiscent of studies on the isostructural CeO_2 material with similar results found for the (111) and (011) surfaces.[99]

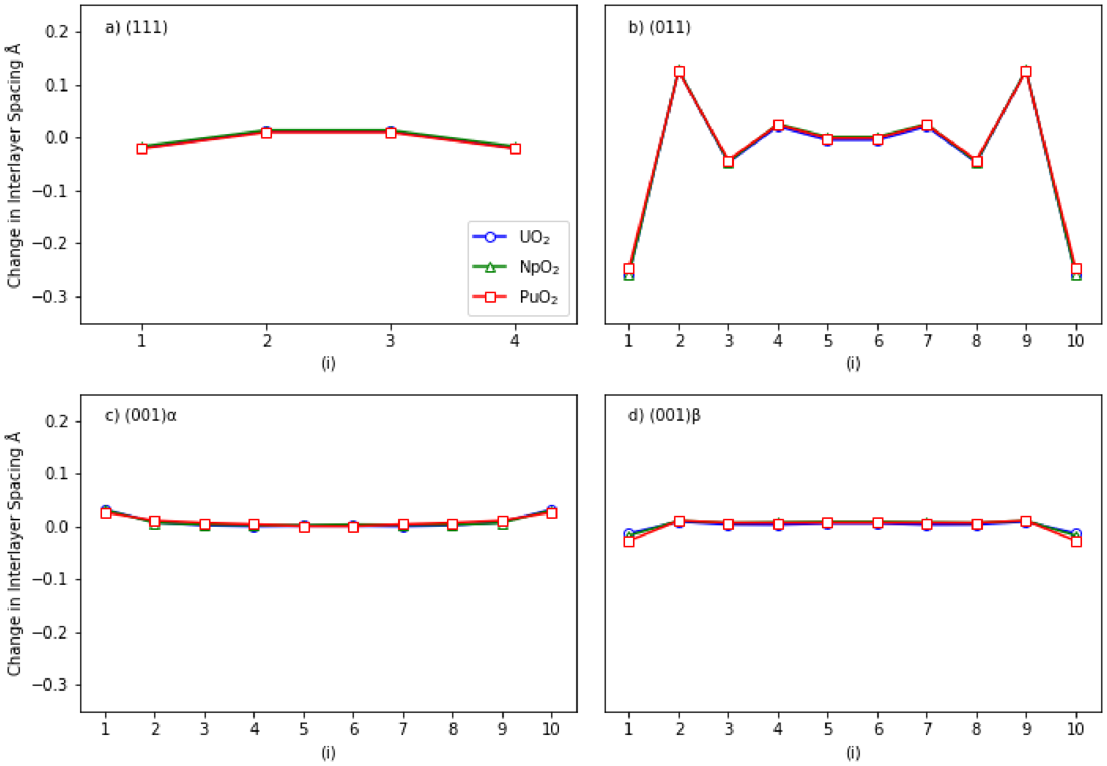

Figure 6: The interlayer An-An relaxation for: (a) (111), (b) (011), (c) (001)α, (d) (001)β surfaces. The interlayer spacing index (i) is indicated in the parentheses.

In the context of An-An relaxation, the (111) surface is marginally distorted. The major difference is confined to the oxygen separation in the second interlayer space. The (011) surface undergoes the greatest overall interlayer relaxation, with the first surface layer experiencing a marked contraction, where the first An layer contracts significantly more than the first O layer.

The contraction of the first layer is countered by a slight expansion of An ions in the second layer, but the bulk structure is regained by the fifth layer. The terminal O ions in the (001)α and (001)β surface undergo a significant contraction, although the remainder of the structure is relatively unaffected. In general, the interlayer relaxation is confined to the first 5 Å, indicating that for investigations of surface reactivity, a slab of minimally 10 Å thick should be used. Our results are similar to those found in studies of CeO_2 and ThO_2.[96]

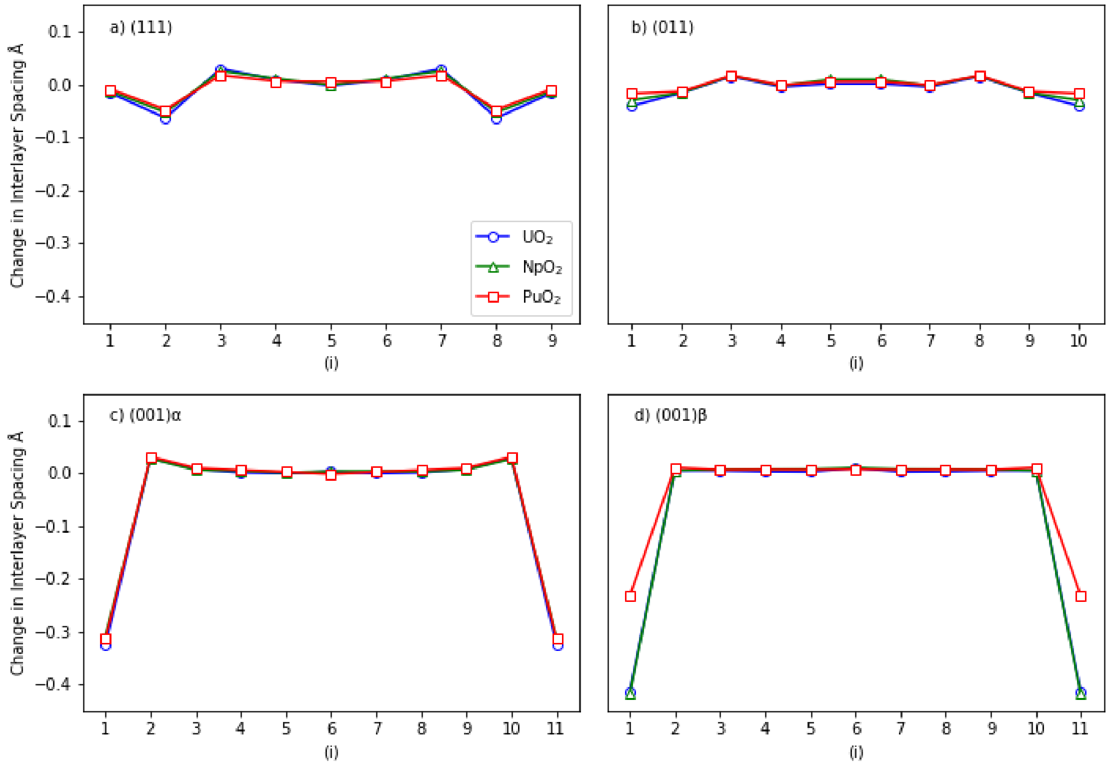

Figure 7: *The interlayer O-O relaxation for: (a) (111), (b) (011), (c) (001)α, (d) (001)β surfaces. The interlayer spacing index (i) is indicated in the parentheses.*

In the context of interlayer O-O relaxation, the distortion of the surface is primarily confined to the first three to four monolayers and the degree of ionic relaxation is generally identical in the AnO_2 surfaces, with the exception of the PuO_2 (001)β surface. In the PuO_2 (001)β surface, the relaxation of the oxygen ions is significantly less relative to the UO_2 and NpO_2 (001)β surfaces. Thus, of the (001)r surfaces, the UO_2 and NpO_2 (001)β surfaces undergo the greatest surface relaxation, whereas in PuO_2, the (001)α surface undergoes the greatest surface relaxation, which is a result of magnetic order and the relaxation in the xy-plane.

No significant structural distortion in the xy-plane occurs in the AnO_2 (111), (011) or (001)α surfaces, possibly as a result of preserving the $Pa\bar{3}$ (No. 205) or $Fm\bar{3}m$ (No. 225) cubic symmetry from the use of noncollinear 3k AFM order.[27] In contrast, the oxygen ions in the UO_2 and NpO_2 (001)β configuration are shifted from their initial positions by the use of transverse 3k AFM ordering (**Figure 8**). This distortion is not observed in the corresponding PuO_2 surface in which the ions are relatively fixed, although there is a minor distortion of the surface plutonium ions, potentially as a consequence of using either transverse 3k AFM or longitudinal 3k AFM behavior. By comparison, the oxygen ions in the (001)αβ configuration are relatively static and, instead, the actinide ion is partially shifted toward the terminal oxygen ions.

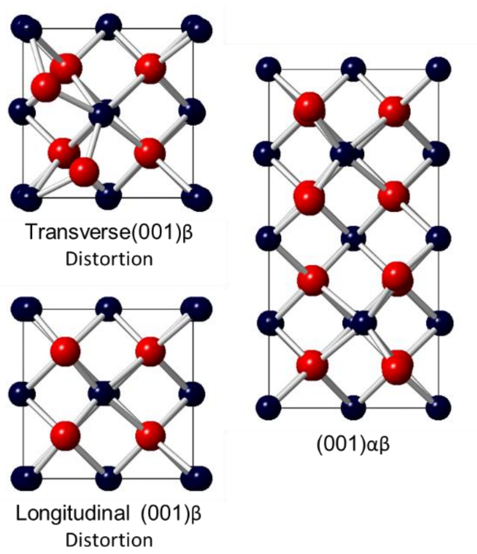

Figure 8: *The ionic relaxation of the low-index AnO$_2$ (001) reconstructed surfaces. The transverse (001)β surface is representative of transverse 3k AFM behavior for UO$_2$ and NpO$_2$, whereas the longitudinal (001)β surface is representative of longitudinal 3k AFM behavior in PuO$_2$. The hybridized (001)αβ surface is calculated regardless of magnetic order for the AnO$_2$. The oxygen (red) and actinide (blue) ions are indicated by the colors in the parentheses.*

3.2 Surface Properties

3.2.1 Electronic Structure

The electronic structure of the AnO$_2$ surfaces has been calculated (**Figure 9**). The covalent nature of the AnO$_2$ materials (a consequence of An (f) and O (p) mixing) is seen to increase along the series. The Mott-Hubbard insulating nature of UO$_2$ is characterized by transitions primarily occurring across the An *f*-bands. Compared to relativistic hybrid DFT calculations of UO$_2$, the calculated band gaps for the low-index surfaces are considerably greater.[15] The charge-transfer insulating nature of PuO$_2$ is characterized by transitions primarily between the valence Pu *f*-band and conduction O *p*-band. In NpO$_2$, both Mott insulating and charge-transfer characteristics are shown in the surface. In general, the electronic structure is only partially perturbed between surfaces.

In addition, the electron affinity and ionization potential of the AnO$_2$ surfaces has been calculated (***Table 2***). This information fills a significant gap in the literature where X-ray photoelectron spectroscopy (XPS) and Kelvin probe microscopy studies have yet to be performed. The electron affinity and the ionization potential increases along the (011) < (111) < (001)β < (001)α series. Of the AnO$_2$ (An = U, Np, Pu) materials, UO$_2$ is the least reactive, whereas PuO$_2$ is the most reactive.

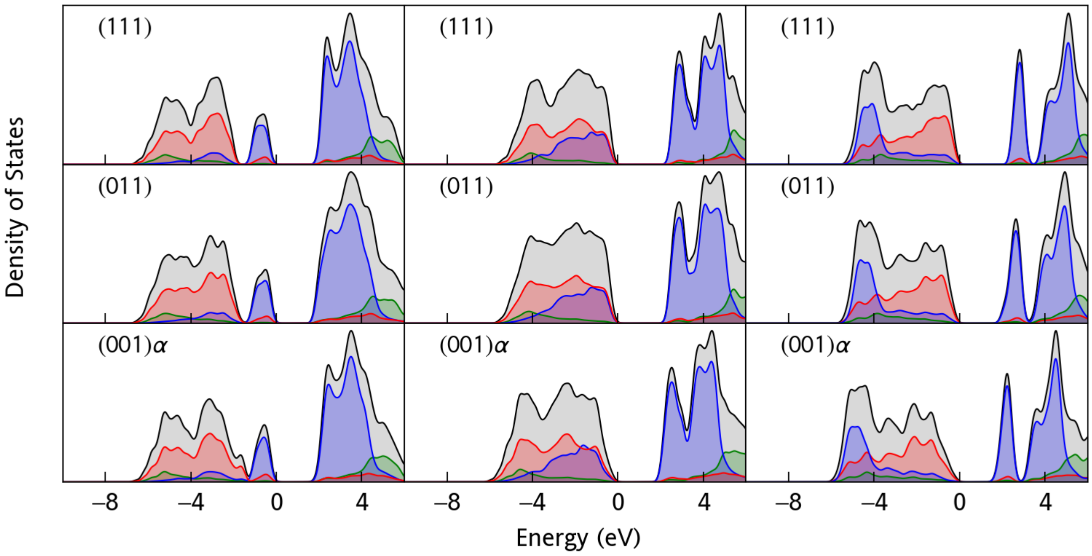

Figure 9: *The calculated density of states for the low-index* AnO_2 *(111), (011), (001)α surfaces; (left)* UO_2*, (center)* NpO_2*, (right)* PuO_2*. The colors in the parentheses indicate the actinide f (blue), actinide d (green) and oxygen p (red) bands. The Fermi level is set at 0 eV.*

Table 2: *The electron affinity (eV), Ionization potential (eV) and Surface energy (J·m^{-2}) for the Low-Index* AnO_2 *Surfaces.*

		(111)	(011)	(001)α	(001)β
UO_2	Electron Affinity (eV)	2.44	1.45	3.69	2.93
	Ionization Potential (eV)	4.54	3.51	5.75	5.00
	Band Gap (eV)	2.11	1.96	2.01	2.15
	Surface Energy (J·m^{-2})	0.85	1.23	1.75	1.83
NpO_2	Electron Affinity (eV)	3.11	2.11	4.33	3.45
	Ionization Potential (eV)	5.98	4.89	7.11	6.23
	Band Gap (eV)	2.64	2.47	2.14	2.50
	Surface Energy (J·m^{-2})	0.90	1.28	1.86	1.92
PuO_2	Electron Affinity (eV)	3.60	1.74	4.89	4.65
	Ionization Potential (eV)	6.45	4.53	7.67	7.44
	Band Gap (eV)	2.58	2.12	1.84	2.03
	Surface Energy (J·m^{-2})	0.92	1.35	1.96	2.13

3.2.2 Magnetic Deviation

The magnetic structure of the low-index AnO_2 surfaces has been investigated. A complete analysis of the actinide ions can be found in the **Additional Information.** The localized magnetic normalized root-mean-square deviation (nRMSD) of the first three monolayers has been calculated for each surface (**Figure 10**). As the monolayer surface depth increases, the magnetic distortion decreases. The total magnetic moment of the U (1.37 μ_B·ion^{-1}), Np (2.70 μ_B·ion^{-1}), and Pu (3.80 μ_B·ion^{-1}) ions remains constant.

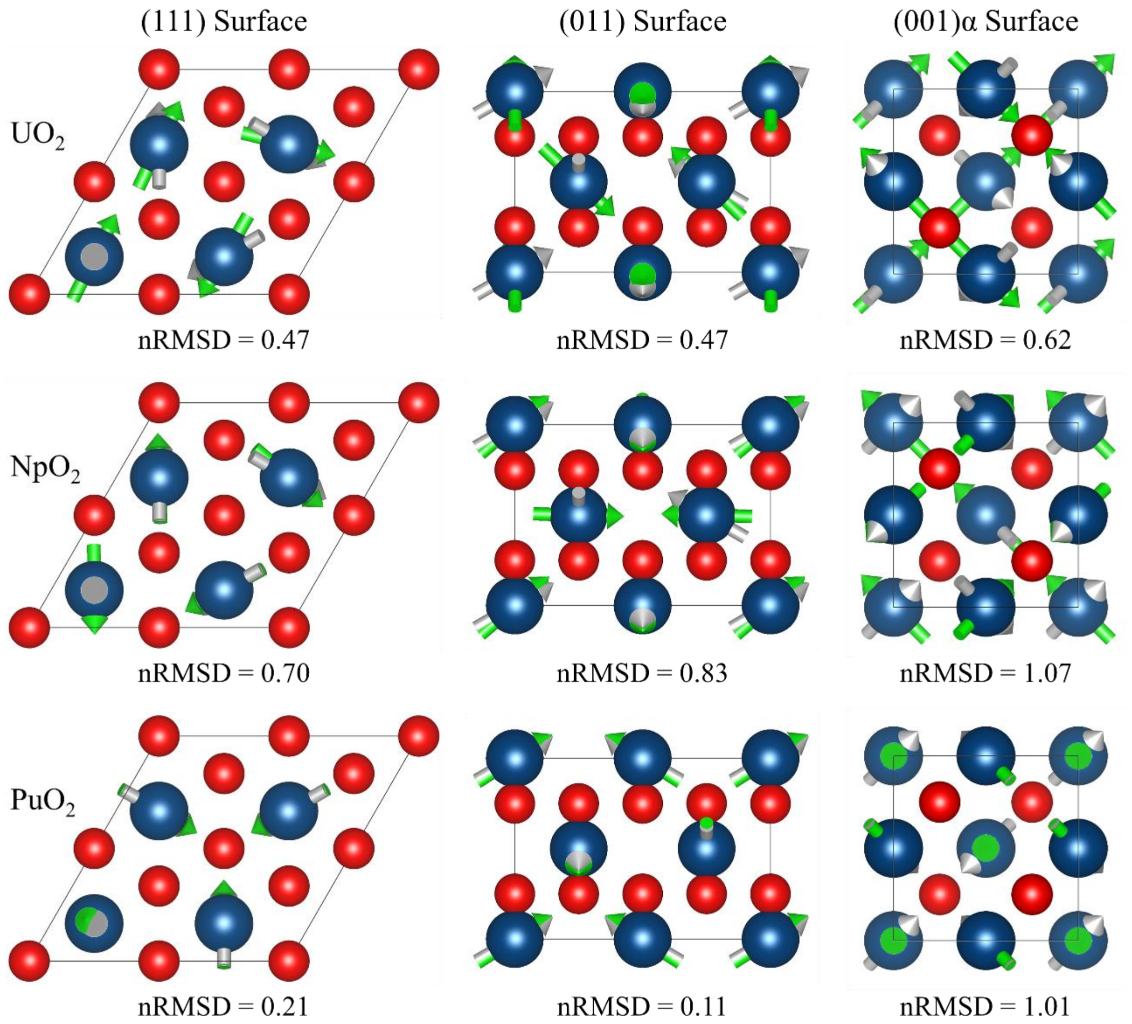

Figure 10: *A cross-sectional illustration of the AnO$_2$ (111), (011), (001)α surfaces for the first three monolayers. The initial magnetic vector (silver), relaxed magnetic vector (green), actinide (blue) and oxygen (red) are shown.*

The comparative localized magnetic deviation in NpO$_2$ for identical surfaces is relatively high. A number of competing low-temperature ($T < 25.4$ K) magnetic states could cause the distortion. For instance, the transverse 3k AFM state, relative to the FM (111) ground-state, is 0.002 eV per formula unit higher in energy; however, no experimental evidence of a FM (111) ground-sate, which results in a $R\bar{3}m$ (No. 166) crystallographic distortion, exists.[25] In addition, the localized magnetic deviation of the (001)α series can be ascribed to the surface instability. In the first three monolayers of the (001)α surface, a FM and an AFM domain are formed. The lowest RMSD is found for the PuO$_2$ (011) surface.

3.2.3 Scanning Tunneling Microscopy

The surface energies of UO$_2$ are extremely sensitive to stoichiometry, defect chemistry, and environmental conditions.[100-102] Low-energy electron diffraction (LEED) measurements of the UO$_2$ (111) surface have identified over 16 individual patterns.[103]. To assist experimental analysis, low-index AnO$_2$ STM images have been calculated (**Figure 11**). The resulting images are analogues to experimental STM studies of AnO_2 surfaces;[86, 104-105] however, in an STM experiment, ionic positions are influenced by perturbations of the electric field caused by the probe. The calculated resolution relative to an experimental study is therefore considerably greater.

The terminal O^{2-} ions are observed in white, whereas the An^{4+} ions area considerably darker. The individual AnO_2 (An = U, Np, Pu) (111), (011) and (001)α surfaces patterns are indistinct. In the (111) surface, the O^{2-} ions result in a hexagonal structure, whereas in the (011) surface, a series of darker channels is observed in one direction. In the (001)α surface, the alignment of the O^{2-} ions results in a diamond pattern. As a means of differentiating between compounds, the (001)β surface is influenced by the magnetic state. In the transverse 3k AFM state for UO_2 and NpO_2, the O^{2-} channels oscillate continuously, whereas in the longitudinal 3k AFM state for PuO_2, the O^{2-} channels are perfectly linear. In other words, the structures can be differentiated by the transverse 3k AFM state of UO_2 and NpO_2 or by the longitudinal 3k AFM state of PuO_2 which is useful information for comparison with future experimental patterns to deduce the magnetic states.

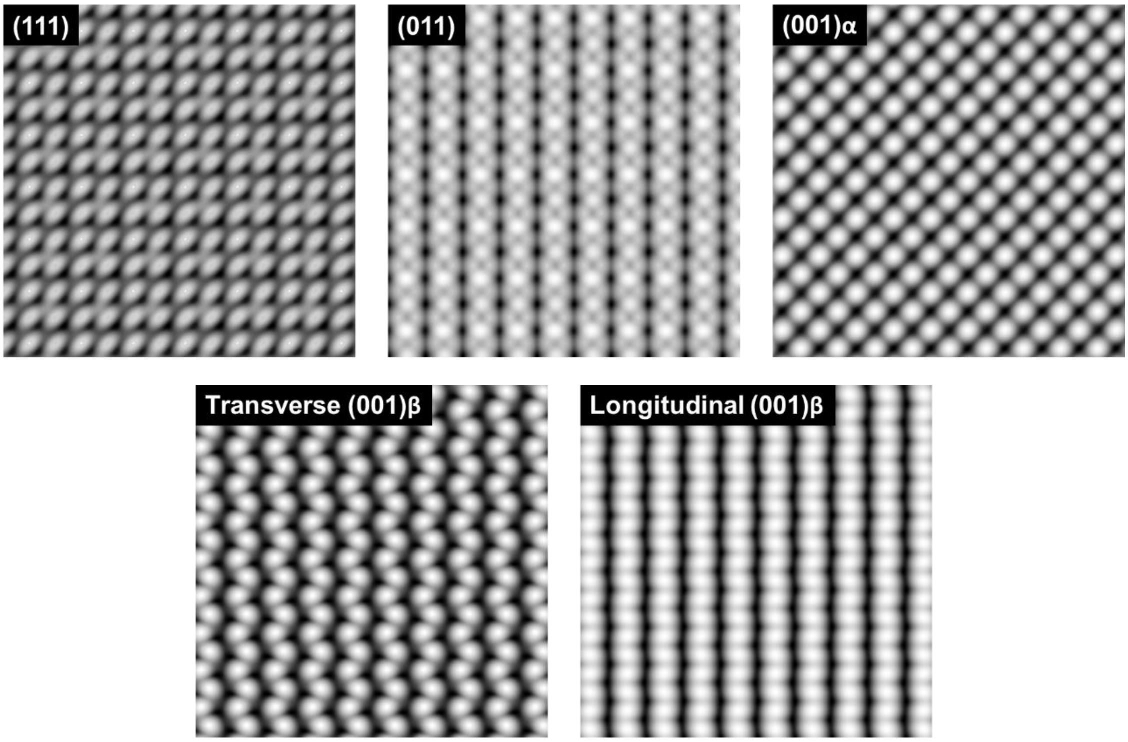

Figure 11: *Low-Index Scanning Tunnelling Microscopy (STM) Images. The AnO_2 (111), (011), (001)α are indistinguishable. The transverse (001)β surface is found for UO_2 and NpO_2; whereas, the longitudinal (001)β surface is found for PuO_2. The terminal O^{2-} ions are observed in white; the An^{4+} ions in dark grey.*

3.2.4 Electrostatic Potential Isosurface

The electrostatic potential isosurface for the low-index AnO_2 surfaces has been calculated using the PBEsol+U functional (**Figure 12**), where the colors indicate regions of relative high (red) and low (blue) charge density. An interesting region of high charge density for an An ion (highlighted in light-blue) on the (111) surface has been identified. The area is expected to have different reaction chemistry compared to the remaining An ions, possibly a site of catalytic activity. In general, regions of high charge density are localized near the oxygen ions. The electrostatic potential isosurfaces of the UO_2 and NpO_2 (001)β differ from that of the PuO_2 (001)β surface, as a consequence of the surface ionic relaxation in the xy-plane, and the surfaces are therefore expected to have different chemical activities.

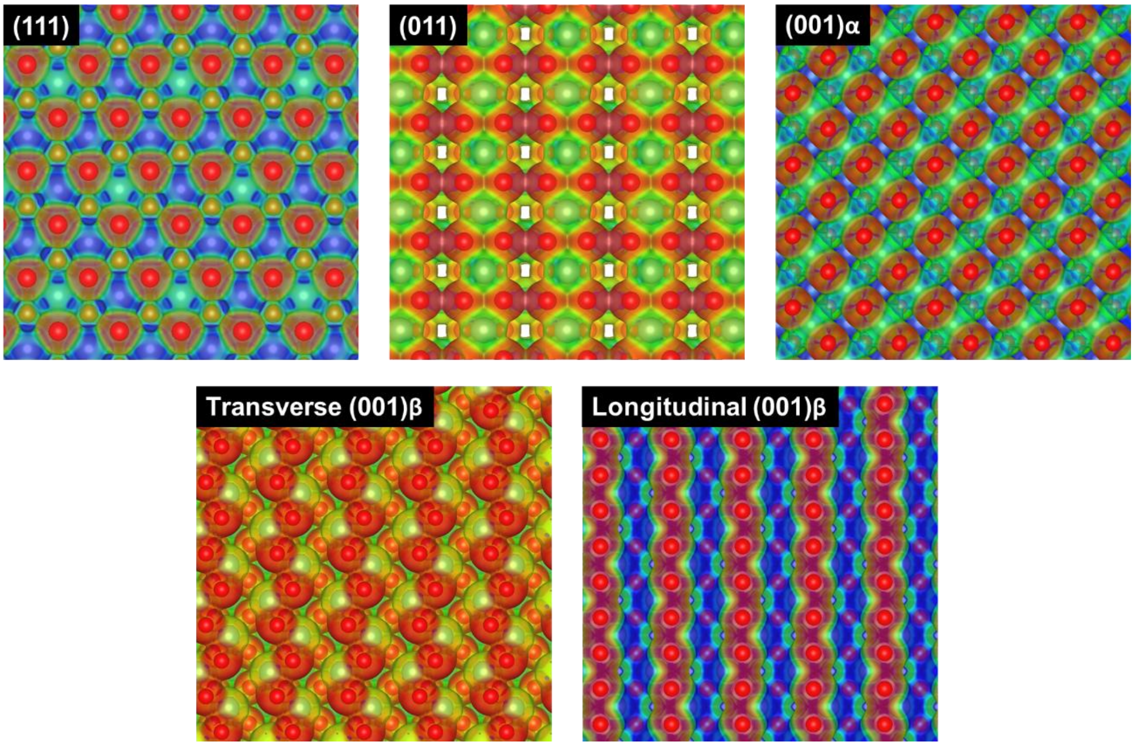

Figure 12: *Electrostatic Potential Isosurfaces. The AnO_2 (111), (011), (001)α are indistinguishable. The transverse (001)β surface is found for UO_2 and NpO_2; whereas, the longitudinal (001)β surface is found for PuO_2. The regions of high and low electrostatic potential are coloured in red and blue, respectively.*

3.2.5 Crystal Morphology

Low-voltage scanning electron microscopy (SEM) of UO_2 has shown a truncated octahedral Wulff crystal morphology,[106] which to our knowledge is the only experimental study concerning the morphology. The truncated octahedral Wulff crystal morphology of UO_2 is inconsistent with studies of other fluorite-type crystal structures and may be the result of environmental influences and the method of sample preparation. The crystals were formed under high pressure (400 MPa) and temperature (1700 °C). A truncated octahedral UO_2 Wulff crystal morphology ($\gamma_{100} = 1.60 \pm 0.02$ J·m^{-2}, $\gamma_{111} = 1.14 \pm 0.03$ J·m^{-2}) has been found; where, empirical interatomic potentials without periodical boundary conditions have been used.[107]

In this study, an octahedral Wulff crystal morphology has been calculated (**Figure 13**) from the surface energies of the low-index (111), (011) and (001)αβ surfaces only. As a result of their relative instabilities, the (001)α and (001)β surface are omitted. Indeed, other high-index surfaces are considerably greater in energy, and their influence on the Wulff crystal morphology is assumed to be negligible.

Figure 13: *The AnO_2 Wulff reconstruction. The crystal structure is formed of (111) facets.*

In terms of computational theory, calculations have shown that the crystal structure is influenced by the magnetic state.[26-27] In theory, the low-temperature octahedral Wulff crystal morphology is linked to the noncollinear 3k AFM state, whereas the high-temperature truncated octahedral Wulff crystal morphology is linked to the PM state. In contrast, the octahedral Wulff crystal morphology of the AnO_2 materials is consistent with fluorite-based materials. The octahedral morphology in the present study is consistent with that calculated by interatomic potentials[89] and with previously reported morphologies for PuO_2[22] and ThO_2[96] calculated by DFT. The (111) surface dominates the morphological features of the particle.

Interatomic potential models of the UO_2 (001) surface have indicated surface configurations of lower energy in a (2·2) unit cell, however this energy is not sufficiently low enough to result in a truncated octahedron.[89] In the calculation of (001) surface energetics, the major limitation is the size of the unit cell and there is therefore a possibility that larger cells may result in a configuration of sufficiently low energy to result in a truncated octahedron. In this study, we have used a (1·1) unit cell with either the (001)α or (001)β configuration, although additional configurations are possible in larger supercells. In theory, one of these surfaces may possess sufficiently low energy to affect the morphology. A systematic investigation of the (2·2) surface is computationally unfeasible, because of the large number of compute-intensive configurations that must be explored.

In another scenario, the experimental sensitivity of UO_2 resulted in a crystal morphology influenced by environmental conditions. It is known that the interaction of oxygen with the AnO_2 surfaces influences the composition range of the solid and the formation of superficial structures.[103] In the past, DFT+U studies have indicated that the truncated crystal morphology is the result of oxygen-rich conditions at 300 K.[108] In addition, interatomic potentials indicate that the AnO_2 (001) surface energy is reduced by hydroxylation,[12, 17] which also results in a truncated octahedron. Other models which use interatomic potentials have obtained an octahedral morphology at thermodynamic equilibrium. However, these studies concluded that the truncated morphology is the result of kinetic limitations.[109] Finally, numerous experimental investigations have shown that the surface energies are temperature-dependent.[100, 110]

4 Conclusions

PBEsol+U has been used to investigate AnO_2 surfaces. In the past, collinear 1k AFM states have been used to model surface structures, but these models predominately use scalar approximations of the crystal electric field which causes an inability to reorient the magnetic vectors relative to the plane of the surface. Therefore, the magnetic structures differ across surface indices. This study considers noncollinear 3k AFM behavior and SOI contributions to the surface energetics of the low-index AnO_2 (111), (011) and (011) surfaces. The magnetic field is carefully re-oriented relative to the plane of the surface for a complete description of the magnetic surface structure. Localized magnetic distortions have also been identified.

The interlayer relaxation of the (111), (011) and (001)α surfaces is confined to the first 5 Å. In contrast to past DFT investigations, our surface energies are considerably higher,[11, 75] which illustrates the important contribution of the SOI[73] to the calculated surface energetics. Our surface energies suggest that the chemical reactivity of the surface has previously been underestimated. The surface stability increases across the (001)β < (001)α < (011) < (111) series, which is typical of CaF_2-type structures. From our Wulff reconstruction, the octahedral crystal morphology is completely dominated by (111) facets. As stated, this is consistent with previous calculations of fluorite-type structures. A computationally tractable method to model the low-index AnO_2 surfaces with improved energetics has been shown.[25] Finally, the models developed and described in this work could be employed in the implementation and use of machine learning methods to investigate structural defects and radiation damage in nuclear fuels.

5 Acknowledgements

This research was supported by the UK Engineering & Physical Science Research Council (EPSRC) (Grant nos. EP/G036675 and EP/K016288) and the Atomic Weapons Establishment Ltd (AWE). AES gratefully acknowledges the United States Department of Homeland Security (DHS), Domestic Nuclear Detection Office (DNDO), National Technical Nuclear Forensics Centre (NTNFC) for a Postdoctoral Research Fellowship. NHdL thanks the Royal Society for an Industry Fellowship and AWE for a William Penney Fellowship. This work made use of the ARCHER UK National Supercomputing Service (http://www.archer.ac.uk), via our membership of the UK's HEC Materials Chemistry Consortium, which is funded by EPSRC (EP/L000202).

6 Supporting Information

Supporting Information Contents: Monolayer Surface Energetics, Fixed Unit Cell Dimensions, Initial Magnetic Structure, Structural Ionic Relaxation, Magnetic Deviation.

7 References

1. Haschke, J. M., Corrosion of Uranium in Air and Water Vapor: Consequences for Environmental Dispersal. *J. Alloys Compd.* **1998**, *278*, 149-160.
2. Haschke, J. M.; Allen, T. H., Plutonium Hydride, Sesquioxide and Monoxide Monohydride: Pyrophoricity and Catalysis of Plutonium Corrosion. *J. Alloys Compd.* **2001**, *320*, 58-71.
3. Haschke, J. M.; Allen, T. H.; Martz, J. C., Oxidation Kinetics of Plutonium in Air: Consequences for Environmental Dispersal. *J. Alloys Compd.* **1998**, *271–273*, 211-215.
4. Haschke, J. M.; Allen, T. H.; Morales, L. A., Reactions of Plutonium Dioxide with Water and Hydrogen–Oxygen Mixtures: Mechanisms for Corrosion of Uranium and Plutonium. *J. Alloys Compd.* **2001**, *314*, 78-91.

5. Haschke, J. M.; Allen, T. H.; Morales, L. A., Surface and Corrosion Chemistry of Plutonium. *Los Alamos Sci.* **2000**, *26*.

6. Haschke, J. M.; Allen, T. H.; Stakebake, J. L., Reaction Kinetics of Plutonium with Oxygen, Water and Humid Air: Moisture Enhancement of the Corrosion Rate. *J. Alloys Compd.* **1996**, *243*, 23-35.

7. Haschke, J. M.; Martz, J. C., Catalyzed Corrosion of Plutonium: Hazards and Applications. *Los Alamos Sci.* **2000**, *26*.

8. Policastro, S.; Martin, F.; Natishan, P.; Moran, P., Corrosion and Corrosion Control. In *Kirk-Othmer Encyclopedia of Chemical Technology*, John Wiley & Sons, Inc.: 2000.

9. Rák, Z.; Ewing, R. C.; Becker, U., Hydroxylation-Induced Surface Stability of AnO_2 (An = U, Np, Pu) from First-Principles. *Surf. Sci.* **2013**, *608*, 180-187.

10. Ewing, R. C.; Runde, W.; Albrecht-Schmitt, T. E., Environmental Impact of the Nuclear Fuel Cycle: Fate of Actinides. *MRS Bull.* **2010**, *35*, 859-866.

11. Bo, T.; Lan, J.-H.; Zhao, Y.-L.; Zhang, Y.-J.; He, C.-H.; Chai, Z.-F.; Shi, W.-Q., Surface Properties of NpO_2 and Water Reacting with Stoichiometric and Reduced NpO_2 (111), (110), and (100) Surfaces From Ab Initio Atomistic Thermodynamics. *Surf. Sci.* **2016**, *644*, 153-164.

12. Abramowski, M.; Redfern, S. E.; Grimes, R. W.; Owens, S., Modification of UO_2 Crystal Morphologies through Hydroxylation. *Surf. Sci.* **2001**, *490*, 415-420.

13. Cakir, P.; Eloirdi, R.; Huber, F.; Konings, R. J. M.; Gouder, T., Surface Reduction of Neptunium Dioxide and Uranium Mixed Oxides with Plutonium and Thorium by Photocatalytic Reaction with Ice. *J. Phys. Chem. C* **2015**, *119*, 1330-1337.

14. Katz, J. J., *The Chemistry of the Actinide and Transactinide Elements (Volumes 1-5)*; Springer Science & Business Media, 2007; Vol. 1.

15. Hoover, M. E.; Atta-Fynn, R.; Ray, A. K., Surface Properties of Uranium Dioxide from First Principles. *J. Nucl. Mater.* **2014**, *452*, 479-485.

16. Matzke, H., *Science of Advanced LMFBR Fuels*; Elsevier Science Pub. Co. Inc.,New York, NY; None, 1986, p Medium: X; Size: Pages: 740.

17. Tan, A. H. H.; Grimes, R. W.; Owens, S., Structures of UO_2 and PuO_2 Surfaces with Hydroxide Coverage. *J. Nucl. Mater.* **2005**, *344*, 13-16.

18. Sun, B.; Liu, H.; Song, H.; Zhang, G.; Zheng, H.; Zhao, X.; Zhang, P., First-Principles Study of Surface Properties of PuO_2: Effects of Thickness and O-Vacancy on Surface Stability and Chemical Activity. *J. Nucl. Mater.* **2012**, *426*, 139-147.

19. Wu, X.; Ray, A. K., A Density Functional Study of Plutonium Dioxide. *Eur. Phys. J. B* **2001**, *19*, 345-351.

20. Sun, B.; Zhang, P.; Zhao, X.-G., First-Principles Local Density Approximation+U and Generalized Gradient Approximation+U Study of Plutonium Oxides. *J. Chem. Phys.* **2008**, *128*, 084705.

21. Jomard, G.; Bottin, F.; Geneste, G., Water Adsorption and Dissociation on the PuO_2 (110) Surface. *J. Nucl. Mater.* **2014**, *451*, 28-34.

22. Jomard, G.; Bottin, F., Thermodynamic Stability of PuO_2 Surfaces: Influence of Electronic Correlations. *Phys. Rev. B* **2011**, *84*, 195469.

23. Moten, S. A.; Atta-Fynn, R.; Ray, A. K.; Huda, M. N., Size Effects on the Electronic and Magnetic Properties of PuO_2 (111) Surface. *J. Nucl. Mater.* **2016**, *468*, 37-45.

24. Boettger, J.; Ray, A., Fully Relativistic Density Functional Calculations on Hydroxylated Actinide Oxide Surfaces. *Int. J. Quantum Chem.* **2002**, *90*, 1470-1477.

25. Pegg, J. T. A Noncollinear Relativistic Computational Study of the Actinide Dioxides and their Interaction with Hydrogen. Engineering Doctorate, UCL (University College London), 2018.

26. Pegg, J. T.; Aparicio-Anglès, X.; Storr, M.; de Leeuw, N. H., DFT+U Study of the Structures and Properties of the Actinide Dioxides. *J. Nucl. Mater.* **2017**, *492*, 269-278.

27. Pegg, J. T.; Shields, A. E.; Storr, M. T.; Wills, A. S.; Scanlon, D. O.; de Leeuw, N. H., Hidden Magnetic Order in Plutonium Dioxide Nuclear Fuel. *Phys. Chem. Chem. Phys.* **2018**, *20*, 20943-20951.

28. van der Laan, G.; Moore, K. T.; Tobin, J. G.; Chung, B. W.; Wall, M. A.; Schwartz, A. J., Applicability of the Spin-Orbit Sum Rule for the Actinide 5f States. *Phys. Rev. Lett.* **2004**, *93*, 097401.

29. Perdew, J. P.; Zunger, A., Self-Interaction Correction to Density-Functional Approximations for Many-Electron Systems. *Phys. Rev. B* **1981**, *23*, 5048-5079.

30. Hohenberg, P.; Kohn, W., Inhomogeneous Electron Gas. *Phys. Rev.* **1964**, *136*, B864-B871.

31. Kohn, W.; Sham, L. J., Self-Consistent Equations Including Exchange and Correlation Effects. *Phys. Rev.* **1965**, *140*, A1133-A1138.

32. Dudarev, S. L.; Botton, G. A.; Savrasov, S. Y.; Humphreys, C. J.; Sutton, A. P., Electron-Energy-Loss Spectra and the Structural Stability of Nickel Oxide: An LSDA+U Study. *Phys. Rev. B* **1998**, *57*, 1505-1509.

33. Liechtenstein, A. I.; Anisimov, V. I.; Zaanen, J., Density-Functional Theory and Strong Interactions: Orbital Ordering in Mott-Hubbard Insulators. *Phys. Rev. B* **1995**, *52*, R5467-R5470.

34. Anisimov, V. I.; Zaanen, J.; Andersen, O. K., Band Theory and Mott Insulators: Hubbard U instead of Stoner I. *Phys. Rev. B* **1991**, *44*, 943-954.

35. Georges, A.; Kotliar, G.; Krauth, W.; Rozenberg, M. J., Dynamical Mean-Field Theory of Strongly Correlated Fermion Systems and the Limit of Infinite Dimensions. *Rev. Mod. Phys.* **1996**, *68*, 13.

36. Adamo, C.; Barone, V., Toward Reliable Density Functional Methods without Adjustable Parameters: The PBE0 Model. *J. Chem. Phys.* **1999**, *110*, 6158-6170.

37. Heyd, J.; Scuseria, G. E.; Ernzerhof, M., Hybrid Functionals Based on a Screened Coulomb Potential. *J. Chem. Phys.* **2003**, *118*, 8207-8215.

38. Prodan, I. D.; Scuseria, G. E.; Martin, R. L., Covalency in the Actinide Dioxides: Systematic Study of the Electronic Properties using Screened Hybrid Density Functional Theory. *Phys. Rev. B* **2007**, *76*, 033101.

39. Caciuffo, R.; Amoretti, G.; Santini, P.; Lander, G. H.; Kulda, J.; Du Plessis, P. d. V., Magnetic Excitations and Dynamical Jahn-Teller Distortions in UO_2. *Phys. Rev. B* **1999**, *59*, 13892-13900.

40. W. M. Jones; Joseph Gordon, E. A. L., The Heat Capacities of Uranium, Uranium Trioxide, and Uranium Dioxide from 15°K to 300°K. *The Journal of Chemical Physics* **1952**, *20*.

41. Huntzicker, J. J.; Westrum, E. F., The Magnetic Transition, Heat Capacity, and Thermodynamic Properties of Uranium Dioxide from 5 to 350 K. *J. Chem. Thermodyn.* **1971**, *3*, 61-76.

42. Arrott, A.; Goldman, J. E., Magnetic Analysis of the Uranium-Oxygen System. *Phys. Rev.* **1957**, *108*, 948-953.

43. Frazer, B.; Shirane, G.; Cox, D.; Olsen, C., Neutron-Diffraction Study of Antiferromagnetism in UO_2. *Phys. Rev.* **1965**, *140*, A1448.

44. Frazer, B.; Shirane, G.; Cox, D.; Olsen, C., First-Order Magnetic Transition in UO_2. *J. Appl. Phys.* **1966**, *37*, 1386-1386.

45. Faber, J.; Lander, G. H.; Cooper, B. R., Neutron-Diffraction Study of UO_2: Observation of an Internal Distortion. *Phys. Rev. Lett.* **1975**, *35*, 1770-1773.

46. Desgranges, L.; Ma, Y.; Garcia, P.; Baldinozzi, G.; Siméone, D.; Fischer, H. E., What Is the Actual Local Crystalline Structure of Uranium Dioxide, UO_2? A New Perspective for the Most Used Nuclear Fuel. *Inorganic Chemistry* **2016**, *56*, 321-326.
47. Dorado, B.; Jomard, G.; Freyss, M.; Bertolus, M., Stability of Oxygen Point Defects in UO_2 by First-Principles DFT+ U Calculations: Occupation Matrix Control and Jahn-Teller Distortion. *Phys. Rev. B* **2010**, *82*, 035114.
48. Faber, J.; Lander, G. H., Neutron Diffraction Study of UO_2: Antiferromagnetic State. *Phys. Rev. B* **1976**, *14*, 1151-1164.
49. Ikushima, K.; Tsutsui, S.; Haga, Y.; Yasuoka, H.; Walstedt, R. E.; Masaki, N. M.; Nakamura, A.; Nasu, S.; Ōnuki, Y., First-Order Phase Transition in UO_2: ^{235}U and ^{17}O NMR Study. *Phys. Rev. B* **2001**, *63*, 104404.
50. Friedt, J. M.; Litterst, F. J.; Rebizant, J., 25-K Phase Transition in NpO_2 from ^{237}Np Mössbauer Spectroscopy. *Phys. Rev. B* **1985**, *32*, 257-263.
51. Erdös, P.; Solt, G.; ⨀ołnierek, Z.; Blaise, A.; Fournier, J. M., Magnetic Susceptibility and the Phase Transition of NpO_2. *Physica B+C* **1980**, *102*, 164-170.
52. Jr., E. F. W.; Hatcher, J. B.; Osborne, D. W., The Entropy and Low Temperature Heat Capacity of Neptunium Dioxide. *The Journal of Chemical Physics* **1953**, *21*, 419-423.
53. Mannix, D.; Lander, G. H.; Rebizant, J.; Caciuffo, R.; Bernhoeft, N.; Lidström, E.; Vettier, C., Unusual Magnetism of NpO_2: A Study with Resonant X-ray Scattering. *Phys. Rev. B* **1999**, *60*, 15187-15193.
54. Caciuffo, R.; Lander, G. H.; Spirlet, J. C.; Fournier, J. M.; Kuhs, W. F., A Search for Anharmonic Effects in NpO_2 at Low Temperature by Neutron Diffraction. *Solid State Commun.* **1987**, *64*, 149-152.
55. Kopmann, W.; Litterst, F. J.; Klauß, H. H.; Hillberg, M.; Wagener, W.; Kalvius, G. M.; Schreier, E.; Burghart, F. J.; Rebizant, J.; Lander, G. H., Magnetic Order in NpO_2 and UO_2 Studied by Muon Spin Rotation. *J. Alloys Compd.* **1998**, *271–273*, 463-466.
56. Santini, P.; Lémanski, R.; Erdős, P., Magnetism of Actinide Compounds. *Adv. Phys.* **1999**, *48*, 537-653.
57. Amoretti, G.; Blaise, A.; Caciuffo, R.; Di Cola, D.; Fournier, J.; Hutchings, M.; Lander, G.; Osborn, R.; Severing, A.; Taylor, A., Neutron-Scattering Investigation of the Electronic Ground State of Neptunium Dioxide. *J. Phys.: Condens. Matter* **1992**, *4*, 3459.
58. Caciuffo, R.; Amoretti, G.; Fournier, J. M.; Blaise, A.; Osborn, R.; Taylor, A. D.; Larroque, J.; Hutchings, M. T., Evidence of a Lattice Distortion in NpO_2 below 25 K from Neutron Magnetic Inelastic Scattering. *Solid State Commun.* **1991**, *79*, 197-200.
59. Spirlet, J. C.; Bednarczyk, E.; Rijkeboer, C.; Rizzoli, C.; Rebizant, J.; Vogt, O., Recent Achievements in Single Crystal Growth of Actinide Compounds. *Inorg. Chim. Acta* **1984**, *94*, 111-112.
60. Wilkins, S. B.; Paixão, J. A.; Caciuffo, R.; Javorsky, P.; Wastin, F.; Rebizant, J.; Detlefs, C.; Bernhoeft, N.; Santini, P.; Lander, G. H., Resonant X-Ray Scattering Study of Magnetic-Dipole and Electric-Quadrupole Order in $U_{0.75}Np_{0.25}O_2$. *Phys. Rev. B* **2004**, *70*, 214402.
61. Tokunaga, Y.; Homma, Y.; Kambe, S.; Aoki, D.; Sakai, H.; Yamamoto, E.; Nakamura, A.; Shiokawa, Y.; Walstedt, R. E.; Yasuoka, H., NMR Evidence for Triple-q Multipole Structure in NpO_2. *Phys. Rev. Lett.* **2005**, *94*, 137209.
62. Wen, X.-D.; Martin, R. L.; Scuseria, G. E.; Rudin, S. P.; Batista, E. R., A Screened Hybrid DFT Study of Actinide Oxides, Nitrides, and Carbides. *J. Phys. Chem. C* **2013**, *117*, 13122-13128.
63. Prodan, I. D.; Scuseria, G. E.; Martin, R. L., Assessment of Metageneralized Gradient Approximation and Screened Coulomb Hybrid Density Functionals on Bulk Actinide Oxides. *Phys. Rev. B* **2006**, *73*, 045104.

64. Andersson, D. A.; Lezama, J.; Uberuaga, B. P.; Deo, C.; Conradson, S. D., Cooperativity among Defect Sites in AO_{2+x} and A_4O_9 (A=U,Np,Pu): Density Functional Calculations. *Phys. Rev. B* **2009**, *79*, 024110.
65. Gryaznov, D.; Heifets, E.; Sedmidubsky, D., Density Functional Theory Calculations on Magnetic Properties of Actinide Compounds. *Phys. Chem. Chem. Phys.* **2010**, *12*, 12273-12278.
66. Yang, Y.; Wang, B.; Zhang, P., Electronic and Mechanical Properties of Ordered $(Pu,U)O_2$ Compounds: A Density Functional Theory +U Study. *J. Nucl. Mater.* **2013**, *433*, 345-350.
67. Zhang, P.; Wang, B.-T.; Zhao, X.-G., Ground-State Properties and High-Pressure Behavior of Plutonium Dioxide: Density Functional Theory Calculations. *Phys. Rev. B* **2010**, *82*, 144110.
68. Gryaznov, D.; Rashkeev, S.; Kotomin, E.; Heifets, E.; Zhukovskii, Y., Helium Behavior in Oxide Nuclear Fuels: First Principles Modeling. *Nucl. Instrum. Methods Phys. Res., Sect. B* **2010**, *268*, 3090-3094.
69. Prodan, I. D.; Scuseria, G. E.; Sordo, J. A.; Kudin, K. N.; Martin, R. L., Lattice Defects and Magnetic Ordering in Plutonium Oxides: A Hybrid Density-Functional-Theory Study of Strongly Correlated Materials. *J. Chem. Phys.* **2005**, *123*, 014703.
70. Jomard, G.; Amadon, B.; Bottin, F.; Torrent, M., Structural, Thermodynamic, and Electronic Properties of Plutonium Oxides from First Principles. *Phys. Rev. B* **2008**, *78*, 075125.
71. Wen, X.-D.; Martin, R. L.; Henderson, T. M.; Scuseria, G. E., Density Functional Theory Studies of the Electronic Structure of Solid State Actinide Oxides. *Chem. Rev.* **2013**, *113*, 1063-1096.
72. Wang, H.; Konashi, K., LDA+U Study of Pu and PuO_2 on Ground State with Spin–Orbital Coupling. *J. Alloys Compd.* **2012**, *533*, 53-57.
73. Steiner, S.; Khmelevskyi, S.; Marsmann, M.; Kresse, G., Calculation of the Magnetic Anisotropy with Projected-Augmented-Wave Methodology and the Case Study of Disordered $Fe_{1-x}Co_x$ Alloys. *Phys. Rev. B* **2016**, *93*, 224425.
74. Bo, T.; Lan, J.-H.; Wang, C.-Z.; Zhao, Y.-L.; He, C.-H.; Zhang, Y.-J.; Chai, Z.-F.; Shi, W.-Q., First-Principles Study of Water Reaction and H_2 Formation on UO_2 (111) and (110) Single Crystal Surfaces. *J. Phys. Chem. C* **2014**, *118*, 21935-21944.
75. Bo, T.; Lan, J.-H.; Zhao, Y.-L.; Zhang, Y.-J.; He, C.-H.; Chai, Z.-F.; Shi, W.-Q., First-Principles Study of Water Adsorption and Dissociation on the UO_2 (111), (110) and (100) Surfaces. *J. Nucl. Mater.* **2014**, *454*, 446-454.
76. Anisimov, V. I., *Strong Coulomb Correlations in Electronic Structure Calculations*; CRC Press, 2000.
77. Monkhorst, H. J.; Pack, J. D., Special Points for Brillouin-Zone Integrations. *Phys. Rev. B* **1976**, *13*, 5188.
78. Blöchl, P. E.; Jepsen, O.; Andersen, O. K., Improved Tetrahedron Method for Brillouin-Zone Integrations. *Phys. Rev. B* **1994**, *49*, 16223.
79. Bousquet, E.; Spaldin, N., J-dependence in the LSDA+U Treatment of Noncollinear Magnets. *Phys. Rev. B* **2010**, *82*, 220402.
80. Suzuki, M. T.; Magnani, N.; Oppeneer, P. M., Microscopic Theory of the Insulating Electronic Ground States of the Actinide Dioxides AnO_2 (An = U, Np, Pu, Am, and Cm). *Phys. Rev. B* **2013**, *88*, 195146.
81. Csonka, G. I.; Perdew, J. P.; Ruzsinszky, A.; Philipsen, P. H.; Lebègue, S.; Paier, J.; Vydrov, O. A.; Ángyán, J. G., Assessing the Performance of Recent Density Functionals for Bulk Solids. *Phys. Rev. B* **2009**, *79*, 155107.

82. Palmer, D. C., Visualization and Analysis of Crystal Structures using CrystalMaker Software. *Z. Physik* **2015**, *230*, 559-572.
83. Momma, K.; Izumi, F., VESTA 3 for Three-Dimensional Visualization of Crystal, Volumetric and Morphology Data. *J. Appl. Crystallogr.* **2011**, *44*, 1272-1276.
84. Watson, G. W.; Kelsey, E. T.; de Leeuw, N. H.; Harris, D. J.; Parker, S. C., Atomistic Simulation of Dislocations, Surfaces and Interfaces in MgO. *J. Chem. Soc., Faraday Trans.* **1996**, *92*, 433-438.
85. Sun, W.; Ceder, G., Efficient Creation and Convergence of Surface Slabs. *Surf. Sci.* **2013**, *617*, 53-59.
86. Muggelberg, C.; Castell, M.; Briggs, G.; Goddard, D., An STM Study of the UO_2 (001) Surface. *Appl. Surf. Sci.* **1999**, *142*, 124-128.
87. Tasker, P., W., The Structure and Properties of Fluorite Crystal Surfaces. *J. Phys. Colloques* **1980**, *41*, C6-488-C6-491.
88. Tasker, P. W., The Stability of Ionic Crystal Surfaces. *J. Phys. C: Solid State Phys.* **1979**, *12*, 4977.
89. Tan, A. H.; Abramowski, M.; Grimes, R. W.; Owens, S., Surface Defect Configurations on the (100) Dipolar Surface of UO_2. *Phys. Rev. B* **2005**, *72*, 035457.
90. Vanpoucke, D. E. P.; Brocks, G., Formation of Pt-Induced Ge Atomic Nanowires on Pt/Ge(001): A Density Functional Theory Study. *Phys. Rev. B* **2008**, *77*, 241308.
91. Vanpoucke, D. E. P.; Brocks, G., Density Functional Theory Study of Pt-Induced Ge (001) Reconstructions. *Phys. Rev. B* **2010**, *81*, 035333.
92. Tersoff, J.; Hamann, D. R., Theory of the Scanning Tunneling Microscope. *Phys. Rev. B* **1985**, *31*, 805-813.
93. Tafreshi, S. S.; Roldan, A.; de Leeuw, N. H., Hydrazine Network on Cu (111) Surface: A Density Functional Theory Approach. *Surf. Sci.* **2015**, *637*, 140-148.
94. Irrera, S.; Roldan, A.; Portalone, G.; De Leeuw, N. H., The Role of Hydrogen Bonding and Proton Transfer in the Formation of Uracil Networks on the Gold (100) Surface: A Density Functional Theory Approach. *J. Phys. Chem. C* **2013**, *117*, 3949-3957.
95. Santos-Carballal, D.; Roldan, A.; Grau-Crespo, R.; de Leeuw, N. H., A DFT Study of the Structures, Stabilities and Redox Behaviour of the Major Surfaces of Magnetite Fe_3O_4. *Phys. Chem. Chem. Phys.* **2014**, *16*, 21082-21097.
96. Shields, A. E.; Santos-Carballal, D.; de Leeuw, N. H., A Density Functional Theory Study of Uranium-Doped Thoria and Uranium Adatoms on the Major Surfaces of Thorium Dioxide. *J. Nucl. Mater.* **2016**, *473*, 99-111.
97. Tian, X.-f.; Wang, H.; Xiao, H.-x.; Gao, T., Adsorption of Water on UO_2 (111) Surface: Density Functional Theory Calculations. *Comput. Mater. Sci.* **2014**, *91*, 364-371.
98. Taylor, T. N.; Ellis, W. P., Distorted Surface Oxygen Structure on UO_2(100). *Surf. Sci.* **1981**, *107*, 249-262.
99. Broqvist, P.; Kullgren, J.; Wolf, M. J.; van Duin, A. C. T.; Hermansson, K., ReaxFF Force-Field for Ceria Bulk, Surfaces, and Nanoparticles. *J. Phys. Chem. C* **2015**, *119*, 13598-13609.
100. Hodkin, E. N.; Nicholas, M. G., Surface and Interfacial Properties of Non-Stoichiometric Uranium Dioxide. *J. Nucl. Mater.* **1977**, *67*, 171-180.
101. Hodkin, E. N.; Nicholas, M. G., Comments on “Surface, Grain Boundary and Interfacial Energies in UO_2 and UO_2-Ni” by P. Nikolopoulos et al. *J. Nucl. Mater.* **1978**, *74*, 178.
102. Hodkin, E. N.; Nicholas, M. G., Surface and Interfacial Properties of Stoichiometric Uranium Dioxide. *J. Nucl. Mater.* **1973**, *47*, 23-30.
103. Ellis, W. P., Low-Energy Electron Diffraction Studies of Uranium Dioxide. *J. Chem. Phys.* **1968**, *48*, 5695-5701.

104. Muggelberg, C.; Castell, M. R.; Briggs, G. A. D.; Goddard, D. T., The Atomic Structure of the UO_2 (111) Surface and the Effects of Additional Surface Oxygen Studied by Elevated Temperature STM. *Surf. Rev. Lett.* **1998**, *05*, 315-320.
105. Castell, M. R.; Dudarev, S. L.; Muggelberg, C.; Sutton, A. P.; Briggs, G. A. D.; Goddard, D. T., Surface Structure and Bonding in the Strongly Correlated Metal Oxides NiO and UO_2. *J. Vac. Sci. Technol., A* **1998**, *16*, 1055-1058.
106. Castell, M. R., Wulff Shape of Microscopic Voids in UO_2 Crystals. *Phys. Rev. B* **2003**, *68*, 235411.
107. Boyarchenkov, A. S.; Potashnikov, S. I.; Nekrasov, K. A.; Kupryazhkin, A. Y., Molecular Dynamics Simulation of UO_2 Nanocrystals Surface. *J. Nucl. Mater.* **2012**, *421*, 1-8.
108. Bottin, F.; Geneste, G.; Jomard, G., Thermodynamic Stability of the UO_2 Surfaces: Interplay between Over-Stoichiometry and Polarity Compensation. *Phys. Rev. B* **2016**, *93*, 115438.
109. Abramowski, M.; Grimes, R. W.; Owens, S., Morphology of UO_2. *J. Nucl. Mater.* **1999**, *275*, 12-18.
110. Nikolopoulos, P.; Nazaré, S.; Thümmler, F., Surface, Grain Boundary and Interfacial Energies in UO_2 and UO_2-Ni. *J. Nucl. Mater.* **1977**, *71*, 89-94.

TOC Graphic: